Spin-resolved electronic response to the phase transition in $MoTe_2$ - Supplemental Material

Andrew P. Weber[1,2,3],* Philipp Rüßmann[4], Nan Xu[1,2], Stefan Muff[1,2], Mauro Fanciulli[1,2], Arnaud Magrez[1], Philippe Bugnon[1], Helmuth Berger[1], Nicholas C. Plumb[2], Ming Shi[2], Stefan Blügel[4], Phivos Mavropoulos[4,5], and J. Hugo Dil[1,2]

[1]*Institute of Physics, École Polytechnique Fédérale de Lausanne, CH-1015, Lausanne, Switzerland*

[2]*Swiss Light Source, Paul Scherrer Institute, CH-5232 Villigen, Switzerland*

[3]*Donostia International Physics Center, 20018 Donostia, Gipuzkoa, Spain*

[4]*Peter Grünberg Institut and Institute for Advanced Simulation, Forschungszentrum Jülich and JARA, 52425 Jülich, Germany and*

[5]*Department of Physics, National and Kapodistrian University of Athens, 15784 Zografou, Greece*

(Dated: September 16, 2018)

* andrew.weber@dipc.org

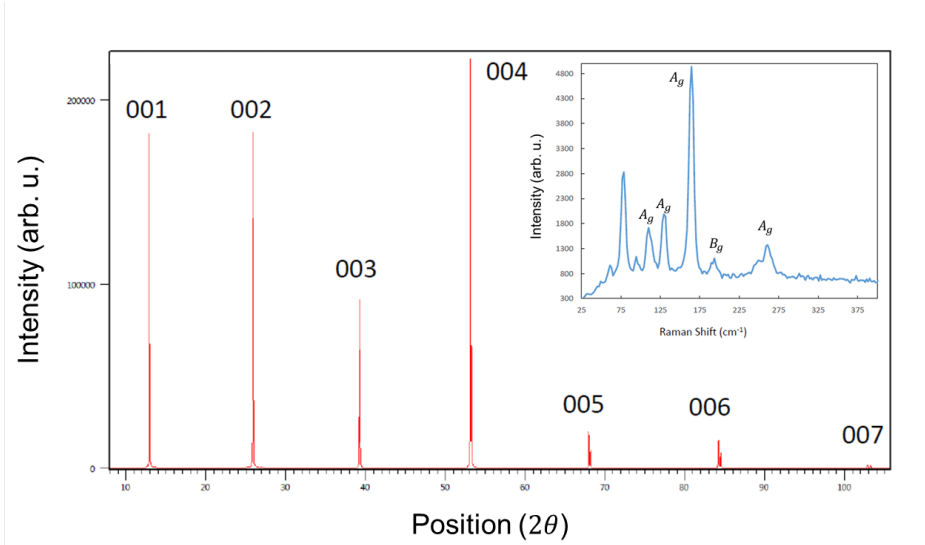

FIG. S1. (Color online) Plot of diffraction intensity versus 2θ using Cu Kα/Kβ source, where 2θ is the angle of detection relative to the beam incidence. (inset) Raman spectral intensity (Stokes lines) versus energy shift. The symmetry and degeneracy of the most relevant Raman modes are indicated in the figure inset. All data were collected with the sample kept at room temperature.

I. CRYSTAL SYNTHESIS AND CHARACTERIZATION

High quality single crystals were grown by chemical vapor transport (CVT). High-purity Mo and Te metals were sealed in a quartz ampule together with iodine used as the transport agent. Optimum crystal growth temperatures were found to be 1000 °C at the source and 940 °C at the drain. The crystal structure was determined to belong to the $P2_1/m$ space group with lattice parameters $a = 6.330$ Å, $b = 3.469$ Å, $c = 10.38600$ Å, and $\beta = 93.92°$ based on reflection-geometry X-ray diffraction using Cu Kα radiation. The 001-007 diffraction peaks are clearly visible, as displayed in the 2θ plot displayed in Fig. S1. The diffraction data and crystal structure refinement results compare well with literature values [62] for 1T'-$MoTe_2$. The structure was further confirmed by Raman scattering spectroscopy using a $\lambda = 532$ nm laser source. The Raman spectrum is shown in the inset of Fig. S1. The presence of the A_g peaks marked in the plot near 113 cm^{-1}, 130 cm^{-1}, 162 cm^{-1}, and 264 cm^{-1} is a strong indication of the monoclinic structure of $MoTe_2$ [63]. The peak near 190 cm^{-1} corresponding to the B_g mode [64] for 1T'-$MoTe_2$ is also visible.

The average stoichiometry of elements in the crystals was determined to be $MoTe_{2\pm0.06}$

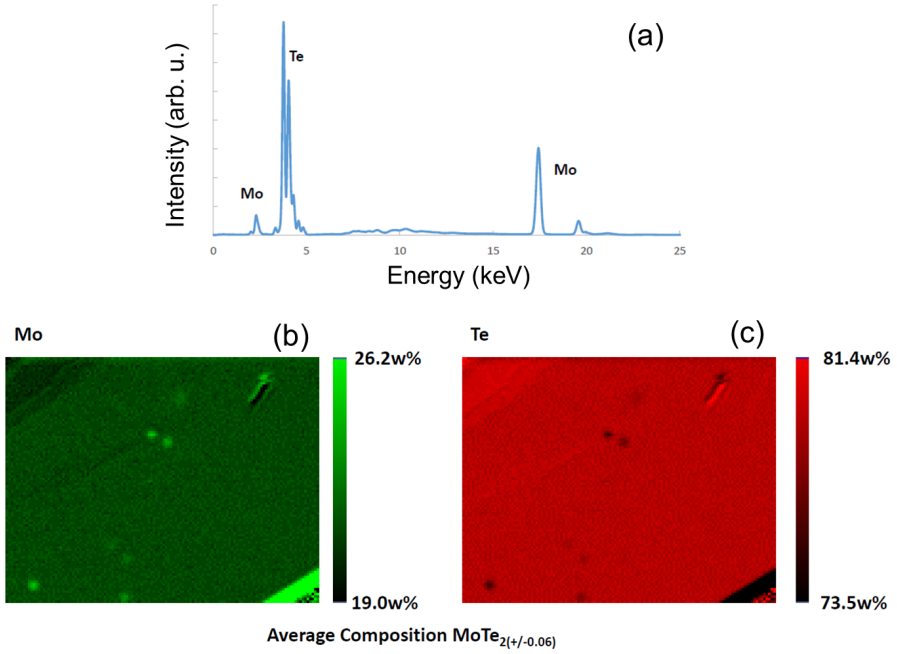

FIG. S2. (Color online) X-ray fluorescence spectro-microscopy data. (a) Representative fluorescence spectrum from the micrographs (b-c) shown below. False-color maps of the percent weight of (b) Mo and (c) Te. The height and width of the micrographs correspond to the 2.3×1.8 mm area of measurement. The corresponding color scales are shown to the right of each panel. All data were collected with the sample kept at room temperature.

by X-ray fluorescence (XRF) microscopy using a Rh source with a spot size of 30 μm, and a beam energy and current of 45 keV and 1.000 A, respectively. A micrograph of 2.3×1.8 mm area was sampled as shown in Fig. S2. Panel (a) shows a representative XRF spectrum from one spot on the micrograph area with peak positions corresponding to Mo and Te labelled. The percent of the total XRF signal in the 0-25 keV energy range contributed by Mo and Te, mapped across the area of the micrograph, is shown by false-color scales in panels (b) and (c), respectively. Overall, the crystal composition is very uniform, with only the presence of several Mo- and Te-rich domains < 100 μm in size and, with exception of a slightly larger Mo-rich wire seen at the lower right of the micrographs.

II. DFT CALCULATIONS

A. Computational Details

We performed our density functional theory calculations using the full-potential relativistic Korringa-Kohn-Rostoker Green function method (KKR). The experimental low-temperature lattice constant for T_d-$MoTe_2$ [7] and the local spin density approximation (LSDA) for the exchange-correlation functional [65] were used. The truncation error arising from the finite angular momentum cutoff of $\ell_{\max} = 3$ used in the calculation was corrected for using Lloyd's formula [66]. The full potential treatment we employed in our calculations includes corrections for the exact shape of the atomic cells [67, 68]. From the converged potentials we computed the Fermi surface and $\boldsymbol{k}$-resolved spin-polarization [69], which were visualized using *Paraview* [70] and the *Matplotlib* library [71] in *python*.

B. Spin-Polarization Magnitude in the Bulk T_d-$MoTe_2$ Fermi Surface.

The magnitude of the spin-polarization vector in the low-temperature phase of $MoTe_2$ is shown on the Fermi surface in Fig. S3. Overall, a high spin-polarization with average values of 70-80% is seen with significantly smaller values only in small regions of the Fermi surface (blue spots in Fig. S3). These regions correspond to so-called "spin-flip hot spots" that are typically close to avoided crossings of different Fermi surface sheets [72].

C. $k_z \to -k_z$ scattering off impurities

To showcase the suppression of scattering for $(k_x, k_y, k_z) \to (k_x, k_y, -k_z)$ due to the odd parity of the P_z, we calculated the elastic scattering rate $P_{\boldsymbol{k}\boldsymbol{k}_0}$ (initial state $\boldsymbol{k}_0$) on the Fermi surface off a Mo-vacancy defect. The vacancy embedding was calculated self-consistently using the Dyson equation to obtain the impurity Green function [73], neglecting structural relaxations (for energetics, lattice relaxations play an important role, but for our qualitative demonstration of spin-dependent scattering strength they are not important). A cluster including the atoms up to the second nearest neighbors were taken into account for a correct screening of the charge density around the impurity. The scattering properties of the vacancy defect were computed based on the calculation of the T-matrix and Fermi's Golden rule using

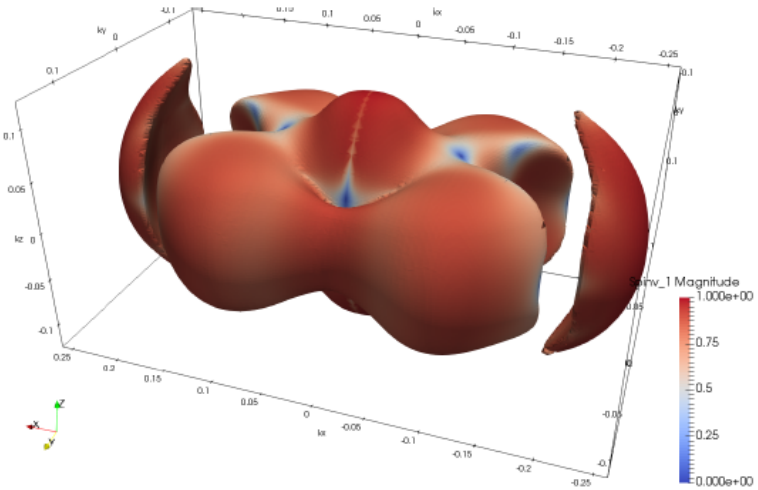

FIG. S3. Magnitude of the spin-polarization in T_d-$MoTe_2$ on the Fermi surface.

the formalism described in ref. [74].

Fig. S4(a) shows the scattering rate off the Mo-vacancy defect for final states on the Fermi surface. The logarithmic color scale highlights that the scattering rate varies strongly within the Fermi surface. Mostly (but not always), small scattering angles (i.e. final states $\boldsymbol{k}$ close to the initial state $\boldsymbol{k}_0$) are favored over large scattering angles, as it was previously seen for example in the surface state of the strong topological insulator (TI) Bi_2Te_3 [28]. In analogy to TI systems, time-reversal symmetry (TRS) leads here to the exact extinction of backscattering into the time-reversal partner state ($\boldsymbol{k}_0 \to -\boldsymbol{k}_0$). To focus on the k_z to $-k_z$ scattering, a cut parallel to the (y, z)-plane passing through $\boldsymbol{k}_0$ is shown in Fig. S4(b), where $P_{\boldsymbol{k}\boldsymbol{k}_0}$ is depicted, and in Fig. S4(c), where P_z is depicted. We find that $(k_x, k_y, k_z) \to (k_x, k_y, -k_z)$ scattering ($\boldsymbol{q}_1$) is two orders of magnitude weaker than $(k_x, k_y, k_z) \to (k_x, -k_y, -k_z)$ scattering ($\boldsymbol{q}_2$). This is well in line with the opposite spin-polarization in the z-component between (k_x, k_y, k_z) and $(k_x, k_y, -k_z)$. Thus, we see that k_z to $-k_z$ scattering is suppressed by the spin-texture even for $\boldsymbol{k}$-points far away from TRS partner.

D. Surface *vs.* Bulk State Spin-Polarization

To compare the symmetries of the spin-polarization of bulk and surface states, the spin-polarization on the Fermi surface of the two non-equivalent surface states (labeled "A" and

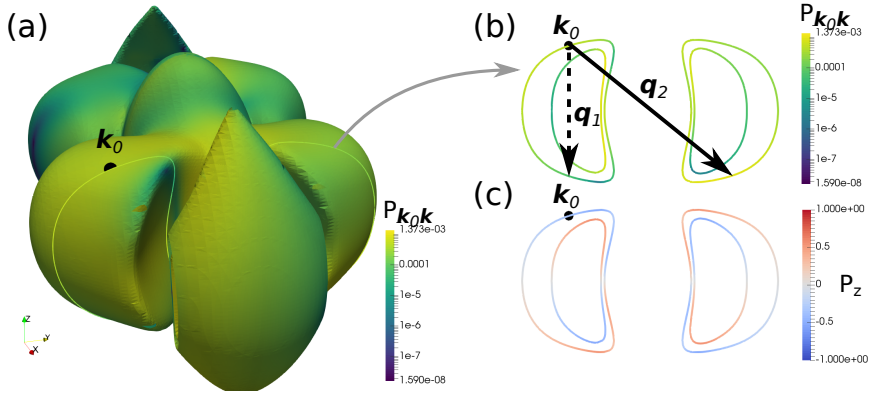

FIG. S4. Scattering properties of a Mo-vacancy defect in T_d-$MoTe_2$. (a) Scattering rate ($P_{\boldsymbol{k}\boldsymbol{k}_0}$ in $\mathrm{fs}^{-1}/\mathrm{at}\%/\mathrm{d}A$ with $\mathrm{d}A$ being the surface area element) for an incident wave $\boldsymbol{k}_0$ (marked with black circle) shown as a logarithmic color plot on the Fermi surface. (b) Cut parallel to the (y, z)-plane crossing $\boldsymbol{k}_0$ showing the scattering rate and (c) the corresponding z-component of the spin (bottom). Scattering with a $\mathbf{q}$-vector $\mathbf{q}_1$ is found to be strongly suppressed due to the non-matching z-component ["blue to red" in (c)] of the spin, while scattering to regions with matching z-component of the spin (e.g. $\mathbf{q}_2$ with "blue to blue") is found to be significantly stronger.

"B" for "top" and "bottom" surfaces) is shown in Fig. S5 for a thin-film system consisting of 8 triple layers (~ 53 thickness) of T_d-$MoTe_2$. A detailed description of the surface geometry and the computational details on the thin-film calculation can be found elsewhere [28].

A symmetry analysis of the surface states compared with the bulk states (Table I) reveals that the z-component of the spin, P_z, has opposite parity in the surface states as compared to the bulk states (even as compared to odd), under the transformation $k_y \to -k_y$ (discussed in the main text). As summarized in Table I, all other components of the spin in the surface state show the same parity as the bulk states with respect to $k_x \to -k_x$ and $k_y \to -k_y$ transformations. Thus the measured spin signals, which were found to compare well with the bulk symmetries, can be associated with bulk-like contribution to the measurement.

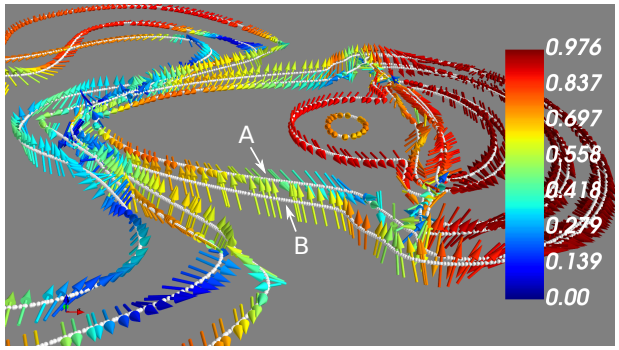

FIG. S5. Fermi surface in the $k_x > 0$ region of the Brillouin zone centered around $(k_x, k_y) = (0.3\,, 0)$ of a ~ 53 thick T_d-$MoTe_2$ film with the direction of the spin-polarization indicated with colored arrows. The color code gives the magnitude of the spin-polarization and the two inequivalent surface states of "top" (A) and "bottom" (B) surfaces are highlighted.

TABLE I. Parity of the spin polarization $P_{x,y,z}$ in bulk and surface states with respect to mirror operations in k-space. While both x and y components have the same parity in bulk and surface states, P_z in the surface state positive parity in the surface states (e.g. state "B" in Fig. S5) and negative in the bulk states (see main text).

	P_x^{bulk}	P_y^{bulk}	P_z^{bulk}	P_x^{surf}	P_y^{surf}	P_z^{surf}
$k_x \to -k_x$	$+$	$-$	$-$	$+$	$-$	$-$
$k_y \to -k_y$	$-$	$+$	$-$	$-$	$+$	$+$
$k_z \to -k_z$	$+$	$+$	$-$	(n.a.)	(n.a.)	(n.a.)

III. SUPPLEMENTARY PHOTOEMISSION DATA

A. Characterization of δ as a topological surface state

In Fig. S6(a) the arc-like constant energy contour of the δ surface state at $E_B = +20$ meV is indicated by a red dashed-line. A SARPES measurement was done at this energy around $k_x = 0.2$ Å^{-1} indicated by markers in the figure. The spin-resolved intensity for P_x in Fig. S6(b) shows a splitting about $k_y = 0$, but the y- and z- channels do not show the same splitting in Fig. S6(c-d). Note that bulk hole states contribute to the signal at higher momenta, contributing a shoulder to the intensity around $k_y = 0.2$ Å^{-1}. The splitting for the x-polarization is expected from the M_y symmetry of both the No. 11 (1T') and No. 31

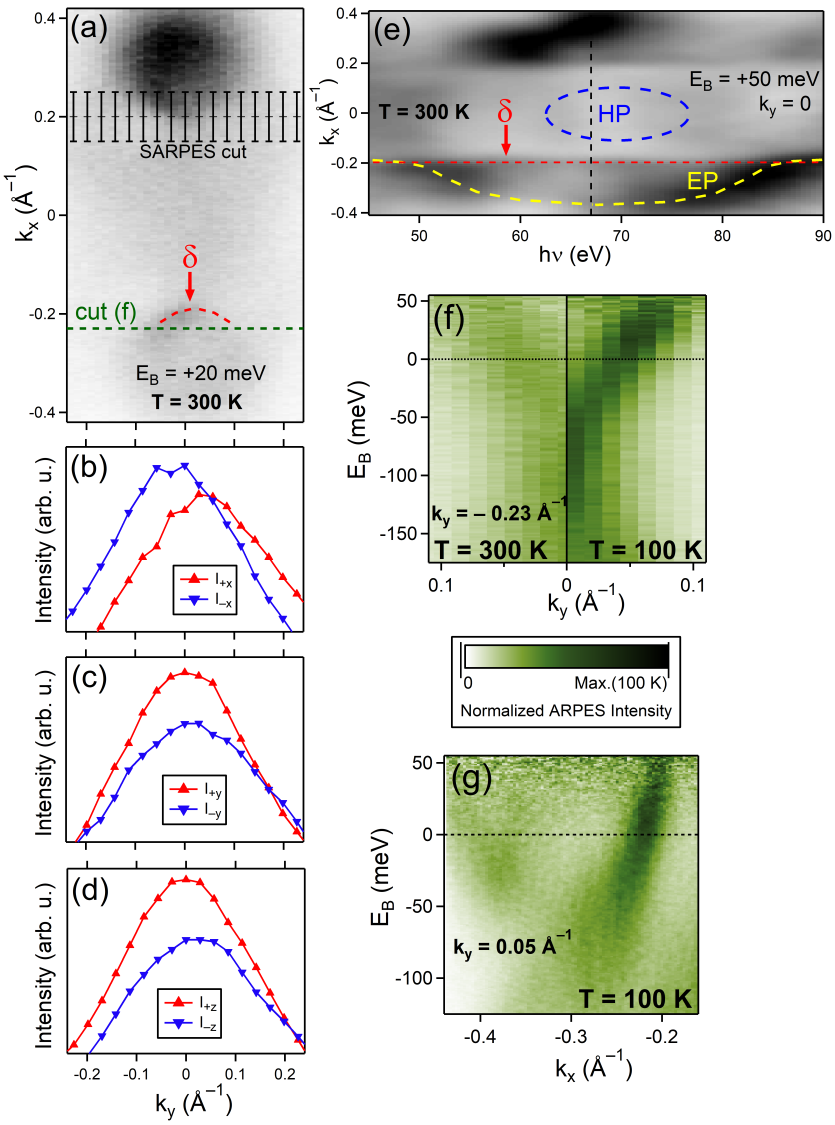

FIG. S6. (S)ARPES intensity maps. (a) Constant energy map at +20 meV collected at $T = 300$ K. (b-d) Spin-resolved intensities along the cut indicated by the black line at the top of panel (a). The error bars around the line in (a) indicate the effective region of integration in momentum space of the SARPES measurement due to the 1.5° angular resolution. (d) Photon energy dependence of the intensity along the k_x-axis at $k_y = 0$ and $E_B = +50$ meV.

(T_d) space groups, but we emphasize the difference of M_y between the two structural cases. In both cases, the reflection is non-symmorphic, but involves a half unit cell translation in the x-direction for the 1T' case and the z-direction for the T_d case. The M_y symmetry is therefore retained or lost on the (001) surface in the 1T' or T_d case, respectively. As

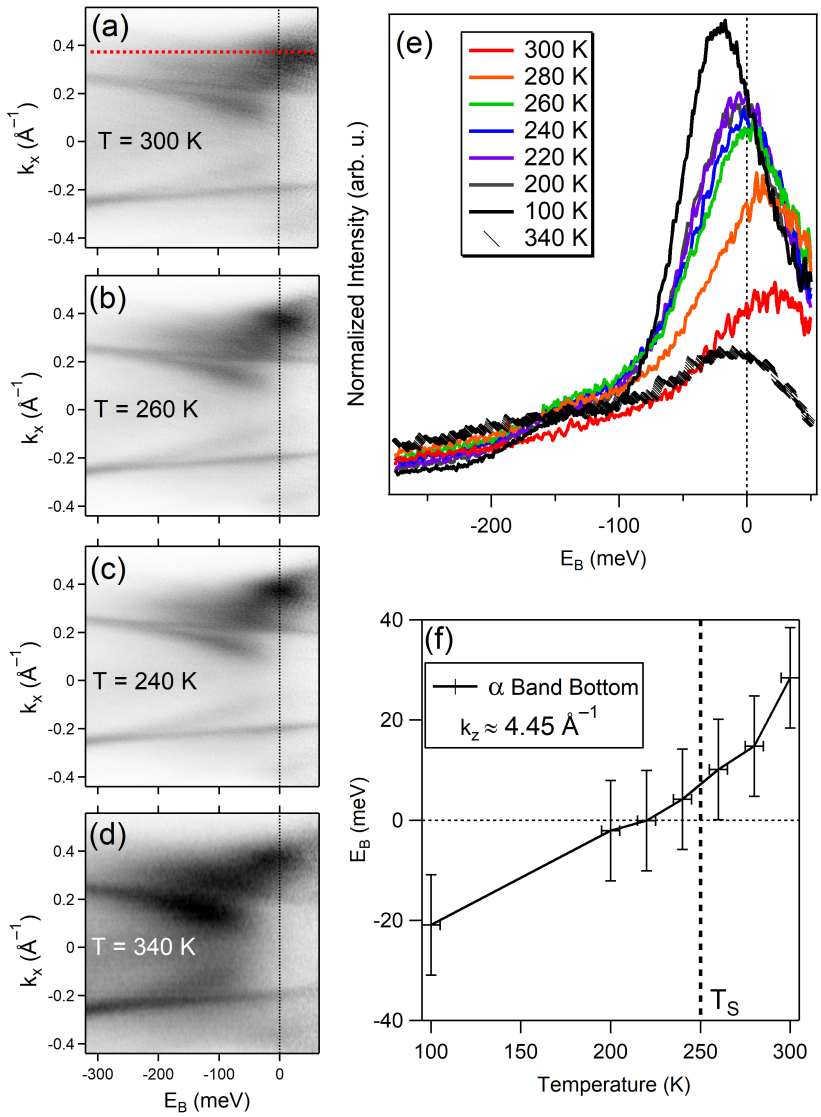

FIG. S7. (a-e) Temperature-dependent ARPES spectra measured using 67 eV photons divided by the Fermi cut-off and (f) binding energy α band bottom.

discussed above, preservation of the sign of P_z upon $k_y \to -k_y$ is a signature of a T_d-phase surface state. This signature is *unique* to the T_d stacking order because finite P_z is forbidden on the 1T' surface by the combination of time-reversal and the M_y symmetry. T_d-like spin-texture is present not only in bulk derived states, as discussed in the main text, but also in the surface state, which further supports the assertion that T_d ordering persists near the surface.

Fig. S6(f) shows the side-by-side comparison of the dispersion along k_y measured at $k_x = -0.23$ Å^{-1} for temperatures of 300 K and 100 K. The spectra have been divided

by the Fermi cutoff and plotted in the same logarithmic color scale (see inset). The state crosses E_F with an electron-like, v-shaped dispersion that is the same for both cases, only the intensity is greatly enhanced at lower temperature. Fig. S6(e) shows the photon-energy dependence of the intensity along k_x at $k_y = 0, E_B = +50$ meV. The surface state appears as a non-dispersive feature (red dashed-line) nestled between dispersive hole-like (blue-dashed line) and electron-like (yellow dashed-line) bulk features, and clearly overlaps with the dispersion of the bulk electron pockets (EPs) for some photon energies. Fig. S7(a-d) further shows that the steep, hole-like dispersion along k_x clearly begins deep within the hole-like bulk bands. Regardless of one's interpretation of the structural or Weyl phase at a given temperature, this state is non-spin-degenerate, non-k_z-dispersive, and is seen to connect (within the resolving capability) the bulk hole- and electron-like bands, and thus meets the definition of a topological surface state. In Fig. S6(g) a dispersion map collected at 100 K and taken along k_x at $k_y = 0.05$ Å^{-1} is shown which compares very well with the data in in Figure 8 of ref. [23] characterizing a so-called candidate topological surface state that is implicated in connecting the Weyl points. We conclude that the state referred to as δ is, or is the precursor of, the state described in that work.

B. Temperature dependent band bending

Fig S7(e) shows energy distribution curves (EDCs) taken at a constant emission angle, corresponding to the red dashed-line in Fig. S7(a), that intersects with the energy minimum of the bulk electron state α at different temperatures, with each spectrum divided by the Fermi cutoff. Upon cooling from $T = 300$ K to 100 K, the peak position clearly shifts from above E_F to below E_F. The results of a double Lorentzian fit (one peak for α and one for the bulk hole states) are shown in Fig. S7(f). The position of α determined from the fit decreases linearly as the temperature is lowered. The error bars are displayed as encompassing a range ± 10 meV, which was always larger than our analyzer resolution and standard deviation of the fitting result added together in quadrature. Upon annealing a cooled sample to 340 K (diagonal black markers), the peak position of α does not move above E_F, and instead lies just a few meV below it. This may be an indication that the lattice polarity requires further heating to be fully removed. Note that Nb-doping was shown to simultaneously decrease the value of T_S and the electron concentration relative to pristine $MoTe_2$. The present results

show further evidence of a relationship between the transition and electron concentration. The Te $4d$ core-levels are also observed shift about 25 meV to higher binding energy upon cooling from 300 to 150 K, as shown in Fig. S8. This again signals an increase in electron density upon cooling. Note that the $J = 3/2$ and $J = 5/2$ levels are each split by a chemical shift of ≈ 0.2 eV that separates the signal of two inequivalent Te atoms in each $MoTe_2$ layer [28].

A possibility exists that the change in electron concentration is enhanced, or perhaps driven, by the adsorption of UHV trace gas such as H_2, which is known to n-dope the surface [75]. The role of molecular adsorption can be logically discounted. Adsorbates introduce scattering centers that would reduce and broaden the ARPES signal, however, the opposite effect is observed; the states become sharper as the temperature is lowered. Gas dosing and sample aging studies would be worthwhile to experimentally show the relative importance of UHV gas adsorption and the underlying lattice polarity in producing such band bending effects.

A photon energy of 67 eV was used in these experiments, which corresponds to a k_z value of around 4.5 Å^{-1}. This is below the Γ point of the 10th BZ, which lies around 4.8 Å^{-1}. As seen in Fig. 1 of the main text, the largest area of the electron Fermi surface, and therefore the energy minimum of the bulk electron states, occurs in the $k_z = 0$ plane, i.e. $k_z = 2\pi n/c$ planes in the full reciprocal space, where n is the BZ index. Therefore, the observation of α lying just above E_F does not mean that the bulk electron states are above E_F elsewhere in the BZ.

C. Self-energy measurements of δ

Fig. S9(a-e) shows detailed information behind the self-energy analysis for cooling a freshly cleaved sample from $T = 300$ K in Fig. 4(c-d) of the main text. It was concluded that the electronic energy-momentum coherence improves significantly upon cooling through T_S in a way that cannot be described in terms of regular thermal broadening. The strength of this conclusion, which was based on the results shown in Fig. 4(c-d) of the main text, can be further appreciated in viewing the raw data in Fig. 3(o-p) of the main text and Fig. S9 of this section. Fig. S9(a) shows the momentum distribution curve (MDC) of δ at E_F measured along k_x (this is the same experimental run as in Fig. 4(c-d) of the main text)

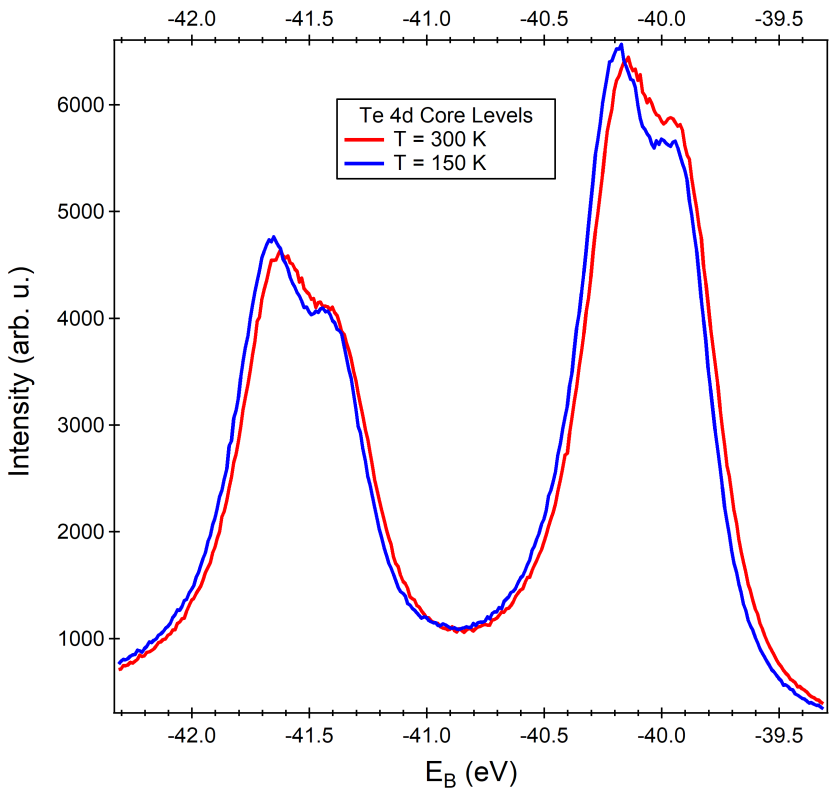

FIG. S8. Temperature-dependent spectra of the Te $4d$ core-levels at normal emission taken using p-polarized 100 eV photons.

for temperatures of $T = 280$, 240, and 200 K. There is little difference in the 240 and 200 K profiles, which indicates a slow rate of change in the momentum-broadening and negligible change in damping of spectral intensity. The profile at 280 K is much less intense than the others and is also broader, its width around half-maximum is visibly close to the width of the 200 and 240 K profile peaks at below their respective half-maxima.

The MDCs of δ along the $k_y = 0$ line were fitted with a Lorentzian profile on a linear background. All of the fitting was done on raw ARPES spectra (energy bin size of 0.795 meV) with no interpolations or other pre-processing. The momentum limits of the fit were placed at -0.13 and -0.29 Å^{-1}. The energy dependence of the extracted momentum coordinates of δ are shown in Fig. S9(b) for $T = 280$, 240, and 200 K. There is essentially no change in the dispersion in cooling from 240 to 200 K. At 280 K, and also 300 K (not shown), the dispersion is distorted relative to the measurements at lower temperatures. The scattering of the momentum coordinates, due to lower signal-to-noise, precludes the detail required to clearly

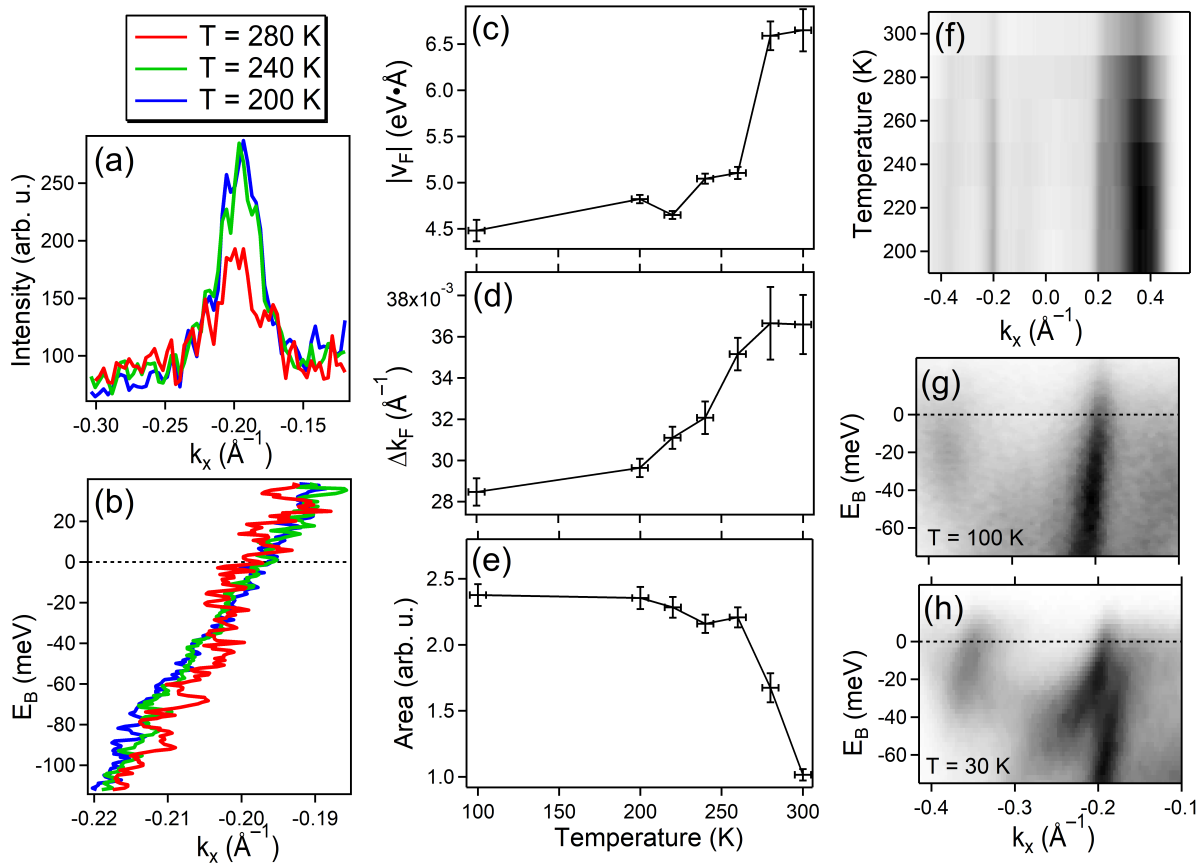

FIG. S9. Temperature dependent ARPES results from data collected using p-polarized 67 eV photons. (a) momentum-distribution curves of ARPES intensity integrated and (b) binding energy dependence of the peak position of δ collected at $k_y = 0$. (c) Fermi velocity, (d) peak width, and (e) peak area obtained from the Lorentzian fit. (f) ARPES intensity at E_F along k_x at $k_y = 0$. Dispersion along k_x at $k_y = 0$ measured at (g) $T = 100$ K and (h) $T = 30$ K. The results in (a-g) were obtained from a sample that was cleaved at 300 K and then cooled. The data in (h) were obtained from a sample that was cleaved and measured at 30 K.

resolve any kink [53] in the dispersion that is a signature of electron-phonon coupling. For the present analysis, a linear dispersion was assumed and the Fermi velocity v_F was obtained from linear fitting of the dispersion over the binding energy interval $-80 < E_B < 20$ meV. Fig. S9(c) shows that the Fermi velocity drops $\approx 30\%$ in magnitude upon cooling from 280 to 260 K, but changes relatively little elsewhere. The decreased magnitude of v_F and the straightening of the dispersion upon cooling could be due to a change of the bare band dispersion and/or the real part of the self-energy.

The photoemission signal is significantly weaker at temperatures above 260 K, which creates a problem for reliable analysis of the quasiparticle peak at a given energy because of low signal-to-noise in the data at hand. This obstacle is overcome by averaging over the width of the Fermi cutoff. Fig. S9(d) and Fig. S9(e) show the temperature dependent peak width Δk_F and area, respectively, obtained by the averaging the respective values extracted from energy slices within the interval $E_F \pm k_B T/2$. The vertical length of the error bars is twice the standard error of the mean. The magnitude of the imaginary part of the self-energy $|\Sigma''(T)|$ shown in Fig. 4(h) of the main text was obtained as $|\Sigma''(T)| = \Delta k_F(T)$, taking the values of Fermi velocity and peak width from the results shown in Fig. S9(c) and Fig. S9(d), respectively. The error bars shown in Fig. 4(h) of the main text were obtained from the error of the results in Fig. S9(c-d) added in quadrature.

Even before taking the Fermi velocity into account, an indication of a change in coherence is manifested in the peak momentum-width (the reciprocal coherence length), where the change between 260 and 240 K is well outside the standard error. The peak area shown in Fig. S9(e) quickly rises to more than twice its initial value upon cooling from 300 to 260 K, which may correspond to reduced damping of the wave-function caused by interactions, and then saturates, which indicates that this damping effect disappears after the crystal has fully transitions into the T_d structural phase. Note that the Swiss Light Source uses top-off injection to maintain a constant current in the electron-storage ring of the synchrotron. Therefore, the intensity of the excitation light remains constant in time for a given beam line condition and there was no need to normalize the ARPES signals for comparison in this case.

The rapid gain of intensity upon cooling to 260 K occurs across the whole Fermi surface. Fig. S9(f) shows a gray-scale image of ARPES intensity along the $k_y = 0$ line integrated over $E_F \pm 5$ meV. The intensity of the bulk electron states appearing strongly around $k_x = 0.4$ Å^{-1}, as well as the intensity of δ appearing around $k_x = \pm 0.2$ Å^{-1} show a similar trend as in Fig. S9(e). Fig. S9(g-h) compare the band structure of δ along the $k_y = 0$ line measured at 100 K and 30 K. A hybridization gap opens at around $E_B = -20$ meV upon cooling below 100 K. This may be an indication of transition to the 4 Weyl point topological phase, wherein the β state is constrained to connect to the bulk hole-like states [23]. In that case, β could hybridize with δ, which is already buried in the projection of these states. Such a band overlap and hybridization could, however, be generically realized through changes in

the surface potential.

D. Response of the Fermi surface and β photoemission signals to cooling

Fig. S10(a-d) shows the temperature dependence of the ARPES intensity measured at E_F. The asymmetry of ARPES intensity in comparing signals from different quadrants of the spectra stems from emission-angle dependence of the photoemission matrix element. The change of this asymmetry seen in comparing panels (a-d) thereby indicates that the orbital characters of the states begin to change even at low temperatures. One can appreciate that the lifetime broadening is significantly enhanced at 300 K, even when compared to the same spectra taken at 200 K. Band dispersion maps along k_y at $k_x = 0.3$ Å^{-1} are shown in Fig. 10(e-h). The ARPES intensity in the V-shaped dispersion of β is very clear at 200 K, but is strongly suppressed around 300 K, which is also the case for the other bands near E_F.

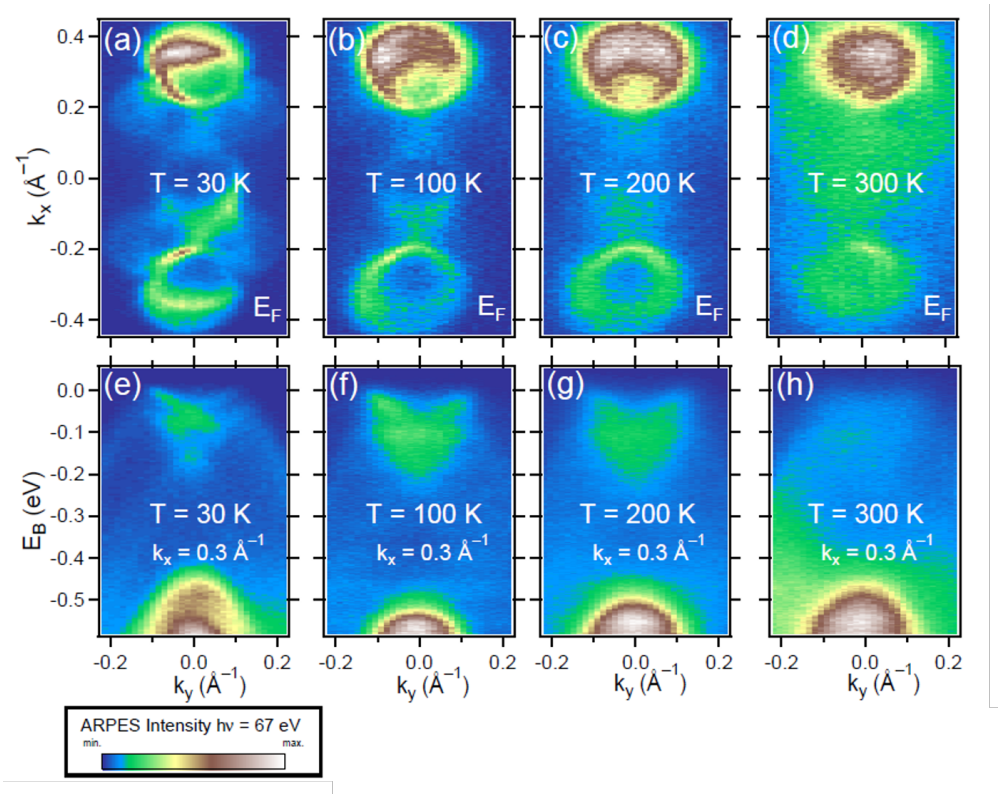

FIG. S10. ARPES intensities of (a-d) the Fermi surface and (e-h) band dispersion along k_y at $k_x = 0.3$ $^{-1}$ measured at (a,e) T = 30 K, (b,f) 100 K, (c,g) 200 K, and (d,h) 300 K.

IV. EXPERIMENTAL DETAILS FOR DATA IN THE MAIN TEXT

Here additional information is provided on the light-polarizations used and the cleaving and temperature histories of the different samples.

All samples were mounted to the sample holder with Ag epoxy and cleaved in UHV by knocking away a post bonded to the top of the sample. The epoxy was cured by heating the sample to 370-400 K, which also ensured that the bulk of $MoTe_2$ was well into the 1T' phase before the experiments began. The SARPES results at $T = 30$ K did not qualitatively depend on the initial cleaving temperature or quality of the sample [47]. In all SARPES measurements, the excitation light was linearly polarized in the x, z-plane (p-polarized light) with an incidence angle of $45 \pm 10°$ relative to the surface normal. Through dipole selection rules, this geometry causes orbitals with even $y \rightarrow -y$ symmetry (e.g. p_x and p_z), and especially orbitals with continuous rotational symmetry (e.g. p_z orbitals) to be preferentially photoexcited [49, 50]. The measured spin-texture therefore transformed under the lattice symmetries almost as if pure spin wave functions were being probed, allowing for direct comparison of the SARPES results with DFT calculations.

For Fig. 2 of the main text, all data were collected from samples cleaved and measured at $T = 30$ K. The data in Fig. 2(a) were collected using right-hand-circular polarized light. The data in Fig. 2(b-e) were collected using p-polarized light. We found that the effect of changed light-polarization (for a given photon energy) produced changes in the photoemission intensities from different states was present but minimal in the energy-momentum space considered. The data in Fig. 2(a), Fig. 2(b-d), and Fig. 2(e) each correspond to different samples or cleaves. The data shown in panels (b-d) were all obtained from the same experimental run (one sample, one cleave).

For the data shown in Fig. 3 of the main text, all data in panels (a-n) were collected using 20 eV photons. The data in panels (a-d), (g-i), and (l-n) were collected from a single sample that was cleaved and measured at 300 K and then cooled over a period of ≈ 1 hour to 30 K. The data in panels (e-f) and (j-k) were collected from separate samples that were cleaved at the same temperature as the measurement. The data in panels (o-p) were collected using 67 eV photons for a single sample cleaved at 300 K and cooled to 100 K over a period of ≈ 7 hours.

To obtain the data shown in Fig. 4 of the main text, only p-polarized 67 eV photons were

used. All data in panels (a) and (c-d) were collected from the same experimental run as in Fig. 3(o-p) of the main text. The spectrum in panel (b) was collected from a sample that was cleaved in UHV at 300 K, placed on the cryo-manipulator and cooled to 120 K (note: in all other experiments the sample was cleaved while mounted on the manipulator), and then annealed to 340 K by controlled counter heating at a rate not exceeding 5 K/min. The pressure rose up to 5×10^{-8} mbar on occasion during the sample transfer and during the heating due to the desorption of gas from the manipulator. This procedure was necessary for a timely experiment. Impurity scattering (likely due to absorbates introduced by the harsh pressure conditions) caused the self-energy broadening to be on the order of 100 meV in the initial measurements at $T = 120$ K for the sample shown in Fig. 4(b). Analysis of self-energy data from full temperature-cycling experiments will be a subject of future work.

The absence of different surface domains in our samples may be due to the thermal gradient and resultant electrostatic potential gradient during cooling. The part of the sample under study must be exposed to vacuum in an ARPES experiment, with the opposite end in direct contact with the cryomanipulator. A thermal gradient therefore exists along the c-axis which also becomes stronger as the temperature is lowered below 300 K. This creates a preferred direction for the phonon transport believed to establish and control the polar ordering and sets up an electrostatic potential gradient on account of the thermopower [4]. Starting from room temperature and cooling down slowly in the presence of this gradient ensures a single phase of T_d-$MoTe_2$ without polar-stacking disorder (provided that dislocations are absent). This scenario will be the same both the case where the sample is cleaved at low temperature (note that the "hot end" of the studied sample corresponds to the "cold end" of the piece which is cleaved away) and the case where the sample is cooled after cleaving at high temperature (polar order of the surface and bulk are established concurrently).

V. COMMENT ON THE APPEARANCE OF BULK-LIKE SPIN-TEXTURE IN β

The spin-texture of surface states in not a main concern of the present work, however, we now discuss the measured spin-polarizations corresponding to the state referred to as β in our main text, which is associated with the (001) surface. Experimentally, the P_z signal of the quasiparticle peaks labelled as β in Fig. 3(d) of the main text changes sign upon reversal of k_y, which is a signature of bulk, rather than surface, character. We note that one

work which combined ultra-high-resolution laser-based ARPES and DFT calculations [33] claimed that the bulk electron state referred to as α in the present work fully overlaps with the β Fermi arc. This claim is in departure from many other reports on $MoTe_2$, including a study that also presented DFT and laser-based ARPES results [23].

Photoemission interference effects may cause discrepancies between computed and spectroscopic spin-texture. However, significant P_z is predicted in DFT calculations for both surface and bulk electrons, whereas large departures from the computed spin-texture normally appear in spin-polarization components which are of null value in the initial states [49, 50, 76, 77]. These effects also strongly depend on photoemission experiment conditions such as the incidence angle, polarization, and energy of the photons, *etc.*. No qualitative change in the spin-polarization was found upon varying such conditions in additional SARPES measurements, which will be shown elsewhere [47]. A second possibility is that the measured P_z derives from the contribution of bulk states to the signal and not from β. The finite resolution of SARPES incorporates signals from states that were not disentangled from that of β in the analysis. Although a good fitting result was achieved, it does not match the raw data exactly or satisfy the requirements of $(P_x, P_y, P_z) \rightarrow (-P_x, P_y, -P_z)$ upon reversal of k_y at a precise, quantitative level. However, it is unlikely that contamination from bulk states left unaccounted for in the analysis was strong enough to produce the apparent discrepancy, given the energy and momentum resolution of the measurement being better than 75 meV and 0.05 Å^{-1}, respectively, and the dominant intensity of β for the low temperature case. For this measurement of the Fermi level spin-polarization, the kinetic energy of the measurement was placed ≈ 25 meV above that of the Fermi level as a way of effectively improving the energy resolution. As the other possibilities can be safely excluded, we conclude from experiment that β inherits a surface resonance character due to hybridization with the bulk. This seems reasonable given the energy-momentum proximity of β and γ.

VI. THE BASIS FOR HIDDEN SPIN-TEXTURE IN 1T'-$MOTE_2$

Any crystal which has at least one non-centrosymmetric atomic site will have so-called hidden spin-polarization in its electronic structure [57]. This is a case wherein each degenerate band $\mathbf{k}$ consists of spatially separated states of equal and opposite spin which are

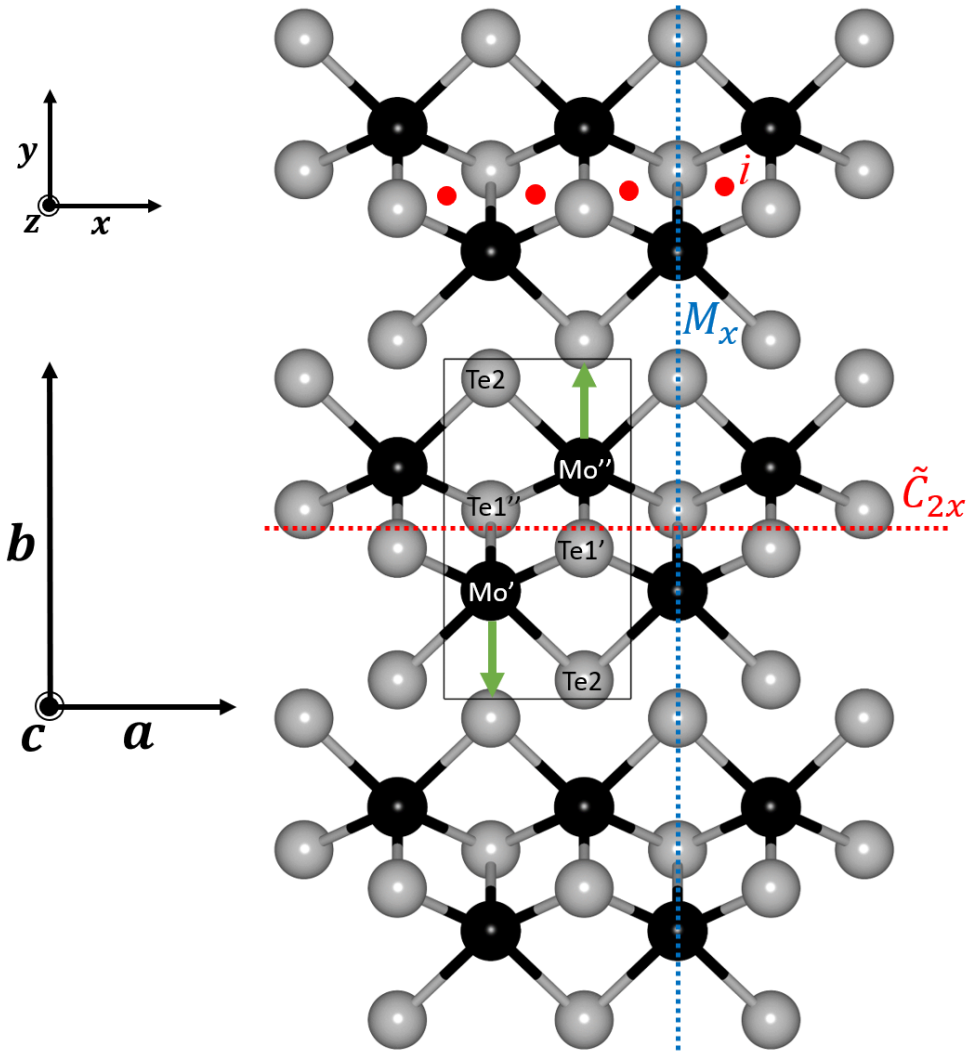

FIG. S11. Ball-and-stick model of monolayer $1T'$-$MoTe_2$ crystal structure, viewed in the ab-plane. Mo and Te atoms are colored in black and gray, respectively. Bonds longer than 2.7 Å are not shown for clarity. The coordinate axes and lattice vectors are shown to the left and the unit cell is displayed as a black, solid-line box. Atoms within the unit cell are labelled as discussed in the text. M_x, $\tilde{C}_{2x}$ symmetry elements are indicated by blue and red dashed-lines, respectively. Inversion sites (labelled i) are indicated by red dots. The orientation of the site dipole field on Mo atoms of different sublattices is indicated by green arrows.

transformed into one another by the inversion operation. Even monolayer 1T'-$MoTe_2$ must have a hidden spin-polarization. A ball-and-stick model of the structure for one monolayer is shown in Fig. S11, looking downward at the xy-plane (ab-plane). There are two types of Te atoms, labelled Te1 and Te2, which are connected to Mo atoms by short and long bonds,

respectively. The Mo atoms form zig-zag chains continuing along the x-direction. All of the atoms in the crystal reside on Wyckoff position $2e$ and have only M_x site symmetry. This corresponds to C_{1v} point group symmetry, which is explicitly mentioned in ref. [57] as a polar point group whose presence in the site symmetry of any atom of the crystal guarantees the existence of so-called R2 (Rashba-two) hidden spin-texture. The reflection symmetry restricts the site dipole fields to be oriented in the y, z-plane. The crystal structure of both monolayer and bulk 1T'-$MoTe_2$ [62] is of space group $P2_1/m$ (no. 11). It contains inversion, the mirror operation M_x, and a screw rotation $\tilde{C}_{2x}$ that consists of 180° rotation about the x-axis and translation in x by a half unit cell. $\tilde{C}_{2x}$ also takes $y \to -y$ and is another form of non-symmorphic M_y symmetry [22], as discussed above. Each set of equivalent atoms (Mo, Te1, Te2) are divided into two sublattices which are transformed into each other by inversion and by $\tilde{C}_{2x}$ [22]. The different sublattice sites for Mo and Te1 are labelled as prime and double prime according to the orientation of the in-plane site dipole field ($-y$ and $+y$, respectively). As indicated by green arrows in Fig. S10 for Mo atoms, the field points along the direction of the longest Mo-Te bond. Indeed, Wannier interpolation analysis of the wave functions obtained in *ab initio* calculations for monolayer WTe_2 (which is isostructural with monolayer 1T'-$MoTe_2$) showed that the electronic charge centers are displaced from the atomic sites [22]. This displacement may be thought of as a response to the site dipole field. Therefore, equal and opposite senses of spin-orbit coupling will exist on the different sublattices.

A well-defined sense of electronic spin-quantization exists in both 1T'- and T_d-$MoTe_2$ in that stationary state of each electron may be written in the form

$$|\uparrow\downarrow\rangle = \sum_i c_i(\mathbf{k})\,|\phi_i\rangle\,|\uparrow\rangle + \sum_j c_j(\mathbf{k})\,|\phi_i\rangle\,|\downarrow\rangle \tag{1}$$

where $c_{i,j}(\mathbf{k})$ are complex coefficients and $|\phi_{i,j}\rangle$ are the orbital functions. A SARPES measurement can be understood as the act of taking spin expectation values from wave functions of this form, except the coefficients are tuned by experiment parameters such as the light-polarization [49, 50]. Hidden spin-texture in other centrosymmetric transition metal dichalcogenides has been revealed by SARPES [78–81], presumably through preferential excitation of one state $|\downarrow\uparrow\rangle$ over its degenerate inversion partner $|\uparrow\downarrow\rangle$. However, photoemission of degenerate states is a very complex process that requires some level of calculation to predict and understand [76, 80, 82]. The present results were found to be insensitive to several

changes to the photon energy and light-polarization [47], but the possibility that the high temperature spin-polarization corresponds to hidden spin-texture cannot be fully excluded. Some level of calculation is needed to determine how the two cases can be distinguished in light-polarization dependent SARPES.

This sublattice dependent spin-polarization is distinct from the case of 2H-MoS_2, wherein oppositely spin-polarized states are well-separated into different layers [79, 80]. Note that hybridization between orbitals on different sublattices merely rotates the spin-polarization vector of the $|\uparrow\downarrow\rangle$ states and does not destroy the hidden spin-texture. Despite the fact that hidden spin-texture must exist in 1T'-$MoTe_2$, it would be very surprising for there to be such little qualitative change in the SARPES measurement (in regard to our comparisons of SARPES data at 300 and 30 K) under a full structural transition. The sublattices, which are equivalent by both inversion and $\tilde{C}_{2x}$ in 1T'-$MoTe_2$, become inequivalent in the T_d phase wherein the intralayer bonding structure changes appreciably [2]. One would expect a large change in spin-orientations to occur upon such a change in bonding, wherein not only the sublattices, but also the $MoTe_2$ layers are coupled in completely different ways. The hidden spin-texture in 1T'-$MoTe_2$ is therefore excluded as the possible source of the high temperature SARPES observations based on this reasoning.

---

[1] R. Clarke, Phil. Mag. B **38** (1978).

[2] S.-Y. Chen, T. Goldstein, D. Venkataraman, A. Ramasubramaniam, and J. Yan, Nano Letters **16**, 5852 (2016).

[3] H. Sakai, K. Ikeura, M. S. Bahramy, N. Ogawa, D. Hashizume, J. Fujioka, Y. Tokura, and S. Ishiwata, Science Advances **2** (2016).

[4] X.-J. Yan, Y.-Y. Lv, L. Li, X. Li, S.-H. Yao, Y.-B. Chen, X.-P. Liu, H. Lu, M.-H. Lu, and Y.-F. Chen, npj Quantum Materials **2**, 31 (2017).

[5] C. Heikes, I.-L. Liu, T. Metz, C. Eckberg, P. Neves, Y. Wu, L. Hung, P. Piccoli, H. Cao, J. Leao, J. Paglione, T. Yildirim, N. P. Butch, and W. Ratcliff, Phys. Rev. Materials **2**, 074202 (2018).

[6] J. He, D. Di Sante, R. Li, X.-Q. Chen, J. M. Rondinelli, and C. Franchini, Nature Communications **9**, 492 (2018).

[7] Y. Qi, P. G. Naumov, M. N. Ali, C. R. Rajamathi, W. Schnelle, O. Barkalov, M. Hanfland, S.-C. Wu, C. Shekhar, Y. Sun, V. Süß, M. Schmidt, U. Schwarz, E. Pippel, P. Werner, R. Hillebrand, T. Förster, E. Kampert, S. Parkin, R. J. Cava, C. Felser, B. Yan, and S. A. Medvedev, Nature Communications **7**, 11038 (2016).

[8] X. Luo, F. C. Chen, J. L. Zhang, Q. L. Pei, G. T. Lin, W. J. Lu, Y. Y. Han, C. Y. Xi, W. H. Song, and Y. P. Sun, Applied Physics Letters **109**, 102601 (2016).

[9] H. Takahashi, T. Akiba, K. Imura, T. Shiino, K. Deguchi, N. K. Sato, H. Sakai, M. S. Bahramy, and S. Ishiwata, Phys. Rev. B **95**, 100501 (2017).

[10] Z. Guguchia, F. von Rohr, Z. Shermadini, A. T. Lee, S. Banerjee, A. R. Wieteska, C. A. Marianetti, B. A. Frandsen, H. Luetkens, Z. Gong, S. C. Cheung, C. Baines, A. Shengelaya, G. Taniashvili, A. N. Pasupathy, E. Morenzoni, S. J. L. Billinge, A. Amato, R. J. Cava, R. Khasanov, and Y. J. Uemura, Nature Communications **8**, 1082 (2017).

[11] A. A. Soluyanov, D. Gresch, Z. Wang, Q. Wu, M. Troyer, X. Dai, and B. A. Bernevig, Nature **527**, 495 (2015).

[12] M. N. Ali, J. Xiong, S. Flynn, J. Tao, Q. D. Gibson, L. M. Schoop, T. Liang, N. Haldolaarachchige, M. Hirschberger, N. P. Ong, and R. J. Cava, Nature **514**, 205 (2014).

[13] Y. Sun, S.-C. Wu, M. N. Ali, C. Felser, and B. Yan, Phys. Rev. B **92**, 161107 (2015).

[14] Z. Wang, D. Gresch, A. A. Soluyanov, W. Xie, S. Kushwaha, X. Dai, M. Troyer, R. J. Cava, and B. A. Bernevig, Phys. Rev. Lett. **117**, 056805 (2016).

[15] Q. L. Pei, W. J. Meng, X. Luo, H. Y. Lv, F. C. Chen, W. J. Lu, Y. Y. Han, P. Tong, W. H. Song, Y. B. Hou, Q. Y. Lu, and Y. P. Sun, Phys. Rev. B **96**, 075132 (2017).

[16] F. C. Chen, H. Y. Lv, X. Luo, W. J. Lu, Q. L. Pei, G. T. Lin, Y. Y. Han, X. B. Zhu, W. H. Song, and Y. P. Sun, Phys. Rev. B **94**, 235154 (2016).

[17] S. Thirupathaiah, R. Jha, B. Pal, J. S. Matias, P. K. Das, P. K. Sivakumar, I. Vobornik, N. C. Plumb, M. Shi, R. A. Ribeiro, and D. D. Sarma, Phys. Rev. B **95**, 241105 (2017).

[18] J. Yang, J. Colen, J. Liu, M. C. Nguyen, G.-w. Chern, and D. Louca, Science Advances **3** (2017).

[19] I. Pletikosić, M. N. Ali, A. V. Fedorov, R. J. Cava, and T. Valla, Phys. Rev. Lett. **113**, 216601 (2014).

[20] J. Jiang, F. Tang, X. C. Pan, H. M. Liu, X. H. Niu, Y. X. Wang, D. F. Xu, H. F. Yang, B. P. Xie, F. Q. Song, P. Dudin, T. K. Kim, M. Hoesch, P. K. Das, I. Vobornik, X. G. Wan, and

D. L. Feng, Physical Review Letters **115**, 166601 (2015).

[21] Q. L. Pei, X. Luo, F. C. Chen, H. Y. Lv, Y. Sun, W. J. Lu, P. Tong, Z. G. Sheng, Y. Y. Han, W. H. Song, X. B. Zhu, and Y. P. Sun, Applied Physics Letters **112**, 072401 (2018).

[22] L. Muechler, A. Alexandradinata, T. Neupert, and R. Car, Phys. Rev. X **6**, 041069 (2016).

[23] A. Tamai, Q. Wu, I. Cucchi, F. Bruno, S. Riccò, T. Kim, M. Hoesch, C. Barreteau, E. Giannini, C. Besnard, A. Soluyanov, and F. Baumberger, Physical Review X **6**, 031021 (2016).

[24] A. Crepaldi, G. Autès, A. Sterzi, G. Manzoni, M. Zacchigna, F. Cilento, I. Vobornik, J. Fujii, P. Bugnon, A. Magrez, H. Berger, F. Parmigiani, O. V. Yazyev, and M. Grioni, Phys. Rev. B **95**, 041408 (2017).

[25] A. Crepaldi, G. Autès, G. Gatti, S. Roth, A. Sterzi, G. Manzoni, M. Zacchigna, C. Cacho, R. T. Chapman, E. Springate, E. A. Seddon, P. Bugnon, A. Magrez, H. Berger, I. Vobornik, M. Kalläne, A. Quer, K. Rossnagel, F. Parmigiani, O. V. Yazyev, and M. Grioni, Phys. Rev. B **96**, 241408 (2017).

[26] D. Rhodes, R. Schönemann, N. Aryal, Q. Zhou, Q. R. Zhang, E. Kampert, Y.-C. Chiu, Y. Lai, Y. Shimura, G. T. McCandless, J. Y. Chan, D. W. Paley, J. Lee, A. D. Finke, J. P. C. Ruff, S. Das, E. Manousakis, and L. Balicas, Phys. Rev. B **96**, 165134 (2017).

[27] N. Xu, Z. J. Wang, A. P. Weber, A. Magrez, P. Bugnon, H. Berger, C. E. Matt, J. Z. Ma, B. B. Fu, B. Q. Lv, N. C. Plumb, M. Radovic, E. Pomjakushina, K. Conder, T. Qian, J. H. Dil, J. Mesot, H. Ding, and M. Shi, (2016), arXiv:1604.02116.

[28] P. Rüßmann, A. P. Weber, F. Glott, N. Xu, M. Fanciulli, S. Muff, A. Magrez, P. Bugnon, H. Berger, M. Bode, J. H. Dil, S. Blügel, P. Mavropoulos, and P. Sessi, Phys. Rev. B **97**, 075106 (2018).

[29] A. N. Berger, E. Andrade, A. Kerelsky, D. Edelberg, J. Li, Z. Wang, L. Zhang, J. Kim, N. Zaki, J. Avila, C. Chen, M. C. Asensio, S.-W. Cheong, B. A. Bernevig, and A. N. Pasupathy, npj Quantum Materials **3**, 2 (2018).

[30] J. Jiang, Z. Liu, Y. Sun, H. Yang, C. Rajamathi, Y. Qi, L. Yang, C. Chen, H. Peng, C.-C. Hwang, S. Sun, S.-K. Mo, I. Vobornik, J. Fujii, S. Parkin, C. Felser, B. Yan, and Y. Chen, Nature Communications **8**, 13973 (2017).

[31] A. Liang, J. Huang, S. Nie, Y. Ding, Q. Gao, C. Hu, S. He, Y. Zhang, C. Wang, B. Shen, J. Liu, P. Ai, L. Yu, X. Sun, W. Zhao, S. Lv, D. Liu, C. Li, Y. Zhang, Y. Hu, Y. Xu, L. Zhao, G. Liu, Z. Mao, X. Jia, F. Zhang, S. Zhang, F. Yang, Z. Wang, Q. Peng, H. Weng, X. Dai,

Z. Fang, Z. Xu, C. Chen, and X. J. Zhou, (2016), arXiv:1604.01706.

[32] K. Deng, G. Wan, P. Deng, K. Zhang, S. Ding, E. Wang, M. Yan, H. Huang, H. Zhang, Z. Xu, J. Denlinger, A. Fedorov, H. Yang, W. Duan, H. Yao, Y. Wu, S. Fan, H. Zhang, X. Chen, and S. Zhou, Nature Physics **12**, 1105 (2016).

[33] L. Huang, T. M. McCormick, M. Ochi, Z. Zhao, M.-T. Suzuki, R. Arita, Y. Wu, D. Mou, H. Cao, J. Yan, N. Trivedi, and A. Kaminski, Nature Materials **15**, 1155 (2016).

[34] M. Sakano, M. S. Bahramy, H. Tsuji, I. Araya, K. Ikeura, H. Sakai, S. Ishiwata, K. Yaji, K. Kuroda, A. Harasawa, S. Shin, and K. Ishizaka, Physical Review B **95**, 121101 (2017).

[35] F. Y. Bruno, A. Tamai, Q. S. Wu, I. Cucchi, C. Barreteau, A. de la Torre, S. McKeown Walker, S. Riccò, Z. Wang, T. K. Kim, M. Hoesch, M. Shi, N. C. Plumb, E. Giannini, A. A. Soluyanov, and F. Baumberger, Physical Review B **94**, 121112 (2016).

[36] I. Belopolski, D. S. Sanchez, Y. Ishida, X. Pan, P. Yu, S.-Y. Xu, G. Chang, T.-R. Chang, H. Zheng, N. Alidoust, G. Bian, M. Neupane, S.-M. Huang, C.-C. Lee, Y. Song, H. Bu, G. Wang, S. Li, G. Eda, H.-T. Jeng, T. Kondo, H. Lin, Z. Liu, F. Song, S. Shin, and M. Z. Hasan, Nature Communications **7**, 13643 (2016).

[37] I. Belopolski, S.-Y. Xu, Y. Ishida, X. Pan, P. Yu, D. S. Sanchez, H. Zheng, M. Neupane, N. Alidoust, G. Chang, T.-R. Chang, Y. Wu, G. Bian, S.-M. Huang, C.-C. Lee, D. Mou, L. Huang, Y. Song, B. Wang, G. Wang, Y.-W. Yeh, N. Yao, J. E. Rault, P. Le Fèvre, F. m. c. Bertran, H.-T. Jeng, T. Kondo, A. Kaminski, H. Lin, Z. Liu, F. Song, S. Shin, and M. Z. Hasan, Phys. Rev. B **94**, 085127 (2016).

[38] C. Wang, Y. Zhang, J. Huang, S. Nie, G. Liu, A. Liang, Y. Zhang, B. Shen, J. Liu, C. Hu, Y. Ding, D. Liu, Y. Hu, S. He, L. Zhao, L. Yu, J. Hu, J. Wei, Z. Mao, Y. Shi, X. Jia, F. Zhang, S. Zhang, F. Yang, Z. Wang, Q. Peng, H. Weng, X. Dai, Z. Fang, Z. Xu, C. Chen, and X. J. Zhou, Physical Review B **94**, 241119 (2016).

[39] Y. Wu, D. Mou, N. H. Jo, K. Sun, L. Huang, S. L. Bud'ko, P. C. Canfield, and A. Kaminski, Physical Review B **94**, 121113 (2016).

[40] J. Sánchez-Barriga, M. G. Vergniory, D. Evtushinsky, I. Aguilera, A. Varykhalov, S. Blügel, and O. Rader, Physical Review B **94**, 161401 (2016).

[41] N. Xu, G. Autès, C. E. Matt, B. Q. Lv, M. Y. Yao, F. Bisti, V. N. Strocov, D. Gawryluk, E. Pomjakushina, K. Conder, N. C. Plumb, M. Radovic, T. Qian, O. V. Yazyev, J. Mesot, H. Ding, and M. Shi, Phys. Rev. Lett. **118**, 106406 (2017).

[42] W. Qisheng, L. Jie, B. Jean, H. Chuang-Han, C. Kaiming, Y. Li, C. Shuai, W. Yang, Z. Wenfeng, W. Kaiyou, C. Tay-Rong, L. Hsin, C. Haixin, and Y. Hyunsoo, Advanced Science (2018).

[43] M. Smidman, M. B. Salamon, H. Q. Yuan, and D. F. Agterberg, Reports on Progress in Physics **80**, 036501 (2017).

[44] B. Feng, Y.-H. Chan, Y. Feng, R.-Y. Liu, M.-Y. Chou, K. Kuroda, K. Yaji, A. Harasawa, P. Moras, A. Barinov, W. Malaeb, C. Bareille, T. Kondo, S. Shin, F. Komori, T.-C. Chiang, Y. Shi, and I. Matsuda, Phys. Rev. B **94**, 195134 (2016).

[45] See Supplemental Material at [URL will be inserted by publisher] for details, which includes Refs. [62-82]

[46] M. Hoesch, T. Greber, V. Petrov, M. Muntwiler, M. Hengsberger, W. Auwärter, and J. Osterwalder, Journal of Electron Spectroscopy and Related Phenomena **124**, 263 (2002).

[47] A.P. Weber *et al.* (In Progress).

[48] O. V. Yazyev, J. E. Moore, and S. G. Louie, Phys. Rev. Lett. **105**, 266806 (2010).

[49] Z. Xie, S. He, C. Chen, Y. Feng, H. Yi, A. Liang, L. Zhao, D. Mou, J. He, Y. Peng, X. Liu, Y. Liu, G. Liu, X. Dong, L. Yu, J. Zhang, S. Zhang, Z. Wang, F. Zhang, F. Yang, Q. Peng, X. Wang, C. Chen, Z. Xu, and X. J. Zhou, Nature Communications **5**, 3382 (2014).

[50] K. Yaji, K. Kuroda, S. Toyohisa, A. Harasawa, Y. Ishida, S. Watanabe, C. Chen, K. Kobayashi, F. Komori, and S. Shin, Nature Communications **8**, 14588 (2017).

[51] F. Meier, H. Dil, J. Lobo-Checa, L. Patthey, and J. Osterwalder, Physical Review B **77**, 165431 (2008).

[52] T. Valla, A. V. Fedorov, P. D. Johnson, and S. L. Hulbert, Phys. Rev. Lett. **83**, 2085 (1999).

[53] P. Hofmann, I. Y. Sklyadneva, E. D. L. Rienks, and E. V. Chulkov, New Journal of Physics **11**, 125005 (2009).

[54] M. Reizer and A. Sergeev, Zh. Eksp. Teor. Fiz. **92**, 2291 (1987).

[55] S. S. Yeh, J. J. Lin, J. Xiunian, and Z. Dianlin, Phys. Rev. B **72**, 024204 (2005).

[56] W.-C. Hsu, C.-C. Chen, Y.-H. Lin, H.-K. Lin, H.-T. Chiu, and J.-J. Lin, Nanoscale Research Letters **7**, 500 (2012).

[57] X. Zhang, Q. Liu, J.-W. Luo, A. J. Freeman, and A. Zunger, Nature Physics **10**, 387 (2014).

[58] H.-J. Kim, S.-H. Kang, I. Hamada, and Y.-W. Son, Phys. Rev. B **95**, 180101 (2017).

[59] R. He, S. Zhong, H. H. Kim, G. Ye, Z. Ye, L. Winford, D. McHaffie, I. Rilak, F. Chen, X. Luo, Y. Sun, and A. W. Tsen, Phys. Rev. B **97**, 041410 (2018).

[60] M. Stengel, D. Vanderbilt, and N. A. Spaldin, Nature Materials **8**, 392 (2009).

[61] K. W. Post, A. S. McLeod, M. Hepting, M. Bluschke, Y. Wang, G. Cristiani, G. Logvenov, A. Charnukha, G. X. Ni, P. Radhakrishnan, M. Minola, A. Pasupathy, A. V. Boris, E. Benckiser, K. A. Dahmen, E. W. Carlson, B. Keimer, and D. N. Basov, Nature Physics , (Online) DOI: 10.1038/s41567 (2018).

[62] B. E. Brown, Acta Crystallographica **20**, 268 (1966).

[63] Y. Sun, Y. Wang, D. Sun, B. R. Carvalho, C. G. Read, C.-h. Lee, Z. Lin, K. Fujisawa, J. A. Robinson, V. H. Crespi, M. Terrones, and R. E. Schaak, Angewandte Chemie International Edition , 2830.

[64] J. C. Park, S. J. Yun, H. Kim, J.-H. Park, S. H. Chae, S.-J. An, J.-G. Kim, S. M. Kim, K. K. Kim, and Y. H. Lee, ACS Nano **9**, 6548 (2015).

[65] S. H. Vosko, L. Wilk, and M. Nusair, Canadian Journal of Physics **58**, 1200 (1980).

[66] R. Zeller, Journal of Physics: Condensed Matter **16**, 6453 (2004).

[67] N. Stefanou, H. Akai, and R. Zeller, Comput. Phys. Commun. **60**, 231 (1990).

[68] N. Stefanou and R. Zeller, J. Phys. : Condensed Matter **3**, 7599 (1991).

[69] B. Zimmermann, P. Mavropoulos, N. H. Long, C.-R. Gerhorst, S. Blügel, and Y. Mokrousov, Physical Review B **93**, 144403 (2016).

[70] U. Ayachit, "The ParaView Guide: A Parallel Visualization Application," (2015).

[71] J. D. Hunter, Computing In Science & Engineering **9**, 90 (2007).

[72] J. Fabian and S. Das Sarma, Phys. Rev. Lett. **81**, 5624 (1998).

[73] D. S. G. Bauer, *Development of a relativistic full-potential first-principles multiple scattering Green function method applied to complex magnetic textures of nano structures at surfaces*, Ph.D. thesis, RWTH Aachen University (2013).

[74] N. H. Long, P. Mavropoulos, B. Zimmermann, D. S. G. Bauer, S. Blügel, and Y. Mokrousov, Physical Review B **90**, 064406 (2014).

[75] J. Seok, J.-H. Lee, S. Cho, B. Ji, H. W. Kim, M. Kwon, D. Kim, Y.-M. Kim, S. H. Oh, S. W. Kim, Y. H. Lee, Y.-W. Son, and H. Yang, 2D Materials **4**, 025061 (2017).

[76] U. Heinzmann and J. H. Dil, Journal of Physics: Condensed Matter **24**, 173001 (2012).

[77] G. Landolt, *Spin-and Angle-Resolved Photoelectron Spectroscopy on Topological Insulators and Bulk Rashba Systems*, Ph.D. thesis, University of Zurich (2014).

[78] J. M. Riley, F. Mazzola, M. Dendzik, M. Michiardi, T. Takayama, L. Bawden, C. Granerød,

M. Leandersson, T. Balasubramanian, M. Hoesch, T. K. Kim, H. Takagi, W. Meevasana, P. Hofmann, M. S. Bahramy, J. W. Wells, and P. D. C. King, Nature Physics , 835.

[79] M. Gehlmann, I. Aguilera, G. Bihlmayer, E. Młyńczak, M. Eschbach, S. Döring, P. Gospodarič, S. Cramm, B. Kardynał, L. Plucinski, S. Blügel, and C. M. Schneider, Scientific Reports **6**, 26197 (2016).

[80] E. Razzoli, T. Jaouen, M.-L. Mottas, B. Hildebrand, G. Monney, A. Pisoni, S. Muff, M. Fanciulli, N. C. Plumb, V. A. Rogalev, V. N. Strocov, J. Mesot, M. Shi, J. H. Dil, H. Beck, and P. Aebi, Phys. Rev. Lett. **118**, 086402 (2017).

[81] W. Yao, E. Wang, H. Huang, K. Deng, M. Yan, K. Zhang, K. Miyamoto, T. Okuda, L. Li, Y. Wang, H. Gao, C. Liu, W. Duan, and S. Zhou, Nature Communications **8**, 14216 (2017).

[82] M. Fanciulli, H. Volfová, S. Muff, J. Braun, H. Ebert, J. Minár, U. Heinzmann, and J. H. Dil, Phys. Rev. Lett. **118**, 067402 (2017).